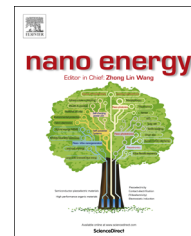




Available online at www.sciencedirect.com

ScienceDirect

journal homepage: www.elsevier.com/locate/nanoenergy



RAPID COMMUNICATION

Lamellar $K_2Co_3(P_2O_7)_2 \cdot 2H_2O$ nanocrystal whiskers: High-performance flexible all-solid-state asymmetric micro-supercapacitors *via* inkjet printing



Huan Pang^{a,b,1}, Yizhou Zhang^{b,1}, Wen-Yong Lai^{b,*},
Zheng Hu^{c,*}, Wei Huang^{b,*}

^aCollege of Chemistry and Chemical Engineering, Yangzhou University, Yangzhou 225002, China

^bKey Laboratory for Organic Electronics and Information Displays (KLOEID) & Institute of Advanced Materials (IAM), Jiangsu National Synergetic Innovation Center for Advanced Materials (SICAM), Nanjing University of Posts & Telecommunications, 9 Wenyuan Road, Nanjing 210023, China

^cKey Laboratory of Mesoscopic Chemistry of MOE, Jiangsu Provincial Lab for Nanotechnology, School of Chemistry and Chemical Engineering, Nanjing University, Nanjing 210093, China

Received 14 February 2015; received in revised form 23 April 2015; accepted 28 April 2015
Available online 9 May 2015

KEYWORDS

Flexibility;
High-performance;
Potassium cobalt
phosphate;
Supercapacitor

Abstract

A flexible all-solid-state asymmetric micro-supercapacitor based on lamellar $(K_2Co_3(P_2O_7)_2 \cdot 2H_2O)$ nanocrystal whiskers and graphene nanosheets was successfully fabricated by inkjet printing in a simple and cost-effective way. A facile method to synthesize lamellar $K_2Co_3(P_2O_7)_2 \cdot 2H_2O$ nanocrystal whiskers under a mild hydrothermal condition was also established. The assembled micro-device exhibited a high specific capacitance (6.0 F cm^{-3}), good rate/mechanical stability and a long cycling stability (5000 cycles) with a maximum energy density of $0.96 \text{ mW h cm}^{-3}$, demonstrating great promise for applications in flexible all-solid-state micro-supercapacitors.

© 2015 Published by Elsevier Ltd.

*Corresponding authors.

E-mail addresses: iamwylai@njupt.edu.cn (W.-Y. Lai), zhenghu@nju.edu.cn (Z. Hu), wei-huang@njtech.edu.cn (W. Huang).

¹The authors contribute equally to this work

Introduction

Portable electronic devices are in urgent need in modern society due to many advantages such as being flexible, ultra-thin and super-light. Efficient micro-energy storage devices are vital for the development of portable electronics. The two main categories of micro-energy storage devices are micro-lithium ion batteries and micro-supercapacitors [1-13]. In the context of portable electronics, micro-supercapacitors are attracting more attention because of their high power density, long cycle lifespan, excellent charge-discharge and environmental-friendly characteristics [14,15]. Supercapacitors can be classified into electric double layer capacitors (EDLCs) and pseudocapacitors on the basis of the charge storage mechanism and the electrode materials. Many carbon-based materials (activated carbon, carbon nanocubes, graphene, etc.) have been developed as electrode materials for EDLCs. However, EDLCs show relatively low capacitance and low energy density [16,17]. Higher energy density can be obtained for micro-devices using pseudo-capacitive electrode materials such as transition metal oxides or conductive polymers whose capacitance mainly come from surface electrochemical reactions [18,19]. However, the micro-device fabrication difficulties and limited selections of materials pose great challenges, and the research on micro-pseudocapacitors is still in its infancy [20,21].

Traditionally, micro-supercapacitors are fabricated via an expensive and extensive lithographic approach. Alternatively, additive fabrication approaches such as inkjet printing offer a simple and versatile route to make complicated planar electrode structure that is crucial for the mass production and the integration into larger systems of micro-supercapacitors. Compared with other printing methods such as screen printing, inkjet printing has advantages in versatility and low cost, and an ease to be integrated into large scale roll-to-roll mass production system. With the rise of printing electronics, there emerge some works on the applications of printing methods for making micro-supercapacitors, mainly on screen printing [21-23], with only few reports on inkjet printing [24-26].

Metal phosphate micro/nano materials have found broad applications in various fields, with the layered metal phosphate/phosphonate being an interesting group of materials [27-30]. Among various phosphates, cobalt-based phosphates which are composed of many layers of connected CoO_x and PO_4 polyhedra (zeolite types), exhibit outstanding electronic/magnetic properties. Due to the layered structure and the redox behaviour of cobalt-based phosphates, these materials hold great promise as electrode materials for electrochemical energy storage devices as was found by our group recently, besides their traditional applications as heterogeneous catalysts, sorbents, ion exchangers, and magnetic materials [31-38]. In spite of some great work, to the best of our knowledge, the exploitation of cobalt phosphate-based micro/nanomaterials for the flexible micro-supercapacitor has not been done yet.

In this work, we report, for the first time, the fabrication of a flexible all-solid-state asymmetric micro-supercapacitor based on lamellar potassium cobalt phosphate hydrate ($\text{K}_2\text{Co}_3(\text{P}_2\text{O}_7)_2 \cdot 2\text{H}_2\text{O}$) nanocrystal whiskers (positive electrode) and graphene nanosheets (negative electrode) using a solid state electrolyte [KOH-polyvinyl alcohol (PVA) gel].

We provide a facile method to synthesize lamellar $\text{K}_2\text{Co}_3(\text{P}_2\text{O}_7)_2 \cdot 2\text{H}_2\text{O}$ nanocrystal whiskers in a mild hydrothermal condition. With the inkjet printing method, complicated planar device structure was easily obtained in a simple and cost-effective way. The assembled micro-device exhibited a high specific capacitance of 6.0 F cm^{-3} at 10 mA cm^{-3} , with a 68.1% retention even at 100 mA cm^{-3} . Furthermore, after over 5000 charge/discharge cycles at 10 mA cm^{-3} , the micro-device only showed small capacitance decay (ca. 5.6%), demonstrating good cycling stability. Due to the highly interconnected structure of the lamellar $\text{K}_2\text{Co}_3(\text{P}_2\text{O}_7)_2 \cdot 2\text{H}_2\text{O}$ nanocrystal whiskers, these nanomaterials exhibited an outstanding mechanical and electrical robustness, which enabled the device to work perfectly well under highly bent conditions. Lastly, a maximum energy density of $0.96 \text{ mW h cm}^{-3}$ for the micro-device has been achieved, which is higher than most previously reported devices with similar structure.

Material and methods

Material preparation

Synthesis of lamellar $\text{K}_2\text{Co}_3(\text{P}_2\text{O}_7)_2 \cdot 2\text{H}_2\text{O}$ nanocrystal whiskers: In a typical synthesis, 0.249 g cobalt acetate, 0.384 g potassium pyrophosphate and 3.730 g potassium chloride were mixed with 15 mL deionized water. The above mixture was stirred for 30 min at room temperature. Then the mixture was transferred into 50 mL stainless-steel autoclaves lined with poly(tetrafluoroethylene) (PTFE, Teflon), which was sealed and maintained at 120°C for 4 h. The obtained precipitates were washed several times by deionized water, ethanol, and dried in the air. The product was directly applied as the positive electrode material.

Preparation of graphite oxide: GO was produced from universal grade, 99.985%-natural graphite powders according to the Hummers' method. Firstly, natural graphite powders were treated with 5% HCl twice, then filtered, washed with distilled water thoroughly, and dried at 110°C for 24 h. Secondly, 10 g graphite powders were added in 230 mL concentrated H_2SO_4 (0°C), then 30 g KMnO_4 was added slowly with stirring and cooling with an ice-water mixture, which held the temperature of the solution at around 20°C . After the solution was stirred for 40 min, 460 mL distilled water was added slowly into the above mixture. The temperature was held at $35 \pm 3^\circ\text{C}$ for 30 min. Finally, distilled water (1.4 L) and 30% H_2O_2 solution (100 mL) were added after the reaction. The solution was held at room temperature overnight and then the mixture was filtered, washed with 5% HCl aqueous solution until sulfate could not be detected with BaCl_2 . The reaction product was dried under vacuum at 50°C for 24 h.

Preparation of functionalized graphene sheets: The dried GO was thermally exfoliated at 300°C for 5 min in the air. The obtained products were subsequently treated at 700°C in Ar for 3 h with a heating rate of $2^\circ\text{C}/\text{min}$. The product was directly applied as the negative electrode material.

The fabrication of flexible all solid-state micro-supercapacitors: Polyethylene terephthalate (PET) ($2.0 \text{ cm} \times 7.0 \text{ cm}$) substrate with a thickness of $100 \mu\text{m}$ was utilized onto which 3 layers of silver ink (ANP Supplies, Korea) as the

current collectors were inkjet printed using a Fujifilm Dimatix 3000 inkjet printer (USA) and dried in a vacuum oven at 100 °C for 1 h. After that, the slurry of active material ($K_2Co_3(P_2O_7)_2 \cdot 2H_2O$) nanocrystal whiskers or graphene nanosheets (see Figure S1 for characterization) was printed by the same printer as the electrode layer on the silver layer and dried in the same vacuum oven at 100 °C for 12 h. The concentration of the $K_2Co_3(P_2O_7)_2 \cdot 2H_2O$ nanocrystal whiskers ink was 0.50 g L⁻¹, and that of graphene nanosheets ink was 2.25 g L⁻¹. It is worth noting that the two inks disperse well in ethanol and remain stable for 7 days (Figure S2). The anodes and cathodes have been printed for 3 layers each. The line width is 70 and 80 μm for the positive and negative electrode, respectively. The subsequent lines overlap with the previous lines well, with only ~5 μm deviation. Three devices were made as parallel experiments. The experiments show good reproducibility. The gel electrolyte (1.52 g PVA, 2.13 g KOH, and 15 mL DI water) was prepared at 75 °C for 30 min and dropped onto the prepared sample to cover the active material after it was cooled naturally. After the electrolyte solidified to a gel, a fresh PET (2.0 cm × 6.0 cm) substrate was used to cover the gel electrolyte as passivation layer in order to make it more stable. After being dried, the device was subjected to electrochemical measurement for the evaluation of its supercapacitor behaviors.

Characterizations

The morphology of as-prepared samples were observed by a JEOL JSM-6701F field-emission scanning electron microscope (FE-SEM) at an acceleration voltage of 5.0 kV, atomic force microscope (AFM) images were measured with CSPM4000 (Benyuan, Beijing), and transmission electron microscopy (TEM) images were captured on the JEM-2100 instrument microscope at an acceleration voltage of 200 kV. The phase analyses of the samples were performed by X-ray diffraction (XRD) on a Rigaku-Ultima III with Cu K α radiation ($\lambda=1.5418 \text{ \AA}$). Nitrogen adsorption-desorption measurements were performed on a Gemini VII 2390 Analyzer at 77 K by using the volumetric method. The specific surface area was obtained from the N₂ adsorption-desorption isotherms and was calculated by the Brunauer-Emmett-Teller (BET) method. The X-ray photoelectron spectroscopy (XPS) spectra were obtained using a PHI5000 Versa Probe.

Electrochemical measurements

Electrochemical study on $K_2Co_3(P_2O_7)_2 \cdot 2H_2O$ nanocrystal whisker electrode: All electrochemical performances were carried out on Arbin-BT2000 electrochemical instrument in a conventional three-electrode system equipped with a platinum electrode, a Hg/HgO electrode as the counter and reference electrode, respectively. Before electrochemical measurements, we have purged out O₂ from the solution by the inert gas-Ar. The working electrode was made by mixing active materials- $K_2Co_3(P_2O_7)_2 \cdot 2H_2O$ nanocrystal whisker, acetylene black, and PTFE (polytetrafluoroethylene) at a weight ratio of 75:15:10, coating on a piece of nickel foam of about 1 cm², and pressing to a thin foil at the pressure of 5.0 MPa. The typical mass load of electrode material was 5.0 mg. The electrolyte was 3.0 M

KOH solutions. Galvanostatic charge-discharge methods were used to investigate the capacitive properties of $K_2Co_3(P_2O_7)_2 \cdot 2H_2O$ nanocrystal whisker electrode, which were all carried out with an Arbin-BT2000 electrochemical instrument. Cyclic voltammetry (CV) and electrochemical impedance spectroscopy measurements of $K_2Co_3(P_2O_7)_2 \cdot 2H_2O$ nanocrystal whisker electrode were conducted at 0.4 V in the frequency range of 100 kHz-0.01 Hz with AC voltage amplitude of 5 mV by using PARSTAT2273.

Electrochemical study of the flexible solid-state micro-supercapacitors: CV measurements were carried out at 5, 10, 20, 30, 50 and 100 mV s⁻¹ between 0 and 1.07 V on an electrochemical work station (PARSTAT2273). The flexible solid-state micro-supercapacitors were galvanostatically charged and discharged at the current density of 10-100 mA cm⁻³ in the voltage range of 0-1.07 V on the Arbin-BT2000 electrochemical instrument. All the electrochemical measurements were conducted at room temperature.

Calculations Method: The capacitance (C) and area-specific capacitance (C_A) of the device can also be calculated using

$$\begin{aligned} C/A = C_A &= Q/(A \times \Delta E) = \int I dt / (A \times \Delta E) \\ &= I \times t_{\text{discharge}} / (A \times \Delta E) \end{aligned} \quad (1)$$

The areal energy density (E) in Wh cm⁻³ and power density (P) in W cm⁻³ derived from galvanostatic charge-discharge curves are calculated from the following expressions:

$$E = C(\Delta E)^2 / (2V \times 3600) \quad (2)$$

$$P = E / t_{\text{discharge}} \quad (3)$$

where A is the surface area of the device, I is the discharge current, $t_{\text{discharge}}$ is discharge time, ΔE is the potential drop during discharge, and V is the volume (cm³) of the device.

Results and discussion

Structural and compositional analysis of as-prepared samples

The XRD pattern of as-prepared sample is shown in Figure 1a. All peaks of the pattern are indexed to be in agreement with $K_2Co_3(P_2O_7)_2 \cdot 2H_2O$ (JCPDS No. 80-1172). There are no peaks from other phosphites or phosphates to be detected. In Figure 1b, the schematic crystal structures of $K_2Co_3(P_2O_7)_2 \cdot 2H_2O$ super cells ($2 \times 2 \times 2$ slabs) are projected based on the data of ICSD-68997. $K_2Co_3(P_2O_7)_2 \cdot 2H_2O$ has layered crystal structure as shown in Figure 1b. A large number of microporous channels have been formed due to the layered crystal structure, which can facilitate the diffusion of ions and electrolytes.

To further analyze the chemical state of the atoms of K, Co, P and O in the samples, XPS was used (Figure S3). In Figure S3a, the signal at 291.7 eV can be attributed to K 2p peak. Besides this major signal, a strong satellite signal at around 294.50 eV was clearly observed, which was the shake-up signal due to multi-electron excitation. In Figure S3b, the signal at 780.3 eV can be assigned to Co 2p_{3/2}, and its shake-up signal was also observed around 785.0 eV-a higher binding energy. The signal at

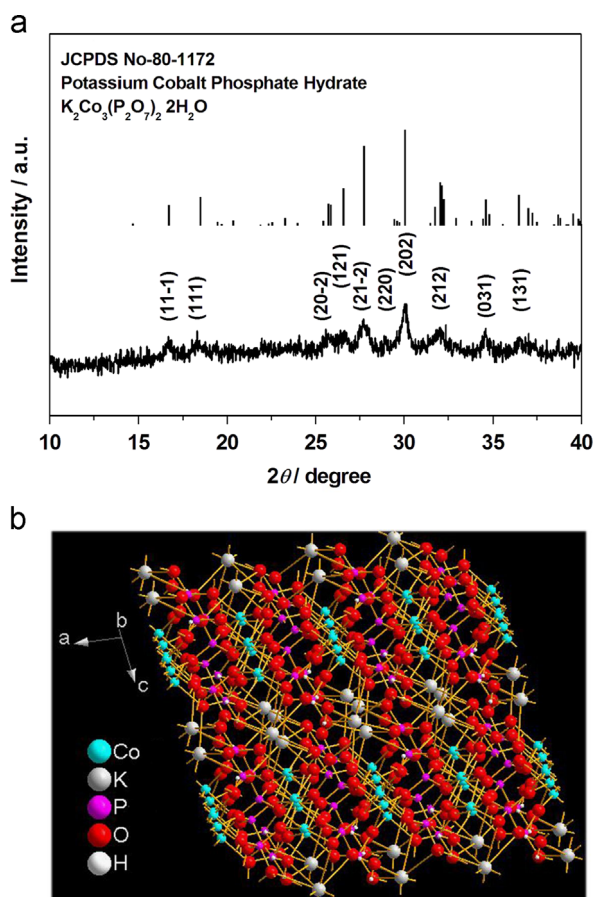


Figure 1 (a) XRD patterns of as-prepared samples and corresponding JCPDS-80-1172; (b) the schematic crystal structures of $K_2Co_3(P_2O_7)_2 \cdot 2H_2O$ super cell ($2 \times 2 \times 2$ slabs) projected based on data of Inorganic Crystal Structure Data (ICSD)-68997.

132.4 eV can be attributed to P 2p peak in Figure S3c. What is more, in Figure S3d the signal of 530.2 eV can be attributed to O 1s.

The morphology of as-prepared $K_2Co_3(P_2O_7)_2 \cdot 2H_2O$ was measured by field emission scanning electron microscopy (FESEM), atomic force microscope (AFM) and transmission electron microscopy (TEM). A typical low-magnification SEM image in Figure 2a shows that the morphology of the as-prepared samples is the nano-whisker with a length of 250–400 nm. The thickness of a single nano-whisker measured by AFM (Figure 2b) is ~ 9.6 nm. The STEM image and EDS mapping images of $K_2Co_3(P_2O_7)_2 \cdot 2H_2O$ nanocrystal whiskers are shown in Figure S4, which further confirm the chemical elemental composition of nanocrystal whiskers. Further, from the TEM image from the side-view of the nanocrystal whisker (Figure 2c), the thickness of a single nanocrystal whisker is ~ 10 nm, consistent with the AFM result in Figure 2b. The measured distance of neighboring lattice fringes (the inset of Figure 2d) is ~ 0.96 nm, twice the (111) lattice spacing (0.479 nm) of $K_2Co_3(P_2O_7)_2 \cdot 2H_2O$, from which we can infer that the $K_2Co_3(P_2O_7)_2 \cdot 2H_2O$ nanocrystal whisker comprises 20–21 single atom layers. A schematic illustration of the layered stacking of the lamellar $K_2Co_3(P_2O_7)_2 \cdot 2H_2O$ nanocrystal whisker is shown in Figure S5, which clearly exhibits the layered model image.

Brunauer-Emmett-Teller (BET) measurements were performed to determine the specific surface area of lamellar $K_2Co_3(P_2O_7)_2 \cdot 2H_2O$ nanocrystal whiskers. The N_2 adsorption-desorption isotherms of the lamellar $K_2Co_3(P_2O_7)_2 \cdot 2H_2O$ nanocrystal whiskers is shown in Figure S6. The BET surface area of the lamellar $K_2Co_3(P_2O_7)_2 \cdot 2H_2O$ nanocrystal whiskers was found to be $89.1 \text{ m}^2 \text{ g}^{-1}$. The pore-size distribution was determined using the Barrett-Joyner-Halenda (BJH) method from the desorption branch of the isotherm in the inset of Figure S6. The average mesopore diameter of the sample is 23 nm, corresponding to the whisker structures assembled or folded, which indirectly confirms the highly interconnected structure of the lamellar $K_2Co_3(P_2O_7)_2 \cdot 2H_2O$ nanocrystal whiskers. The micropore diameter of the sample is about 1.0 nm calculated from the H-K model, which is also consistent with the HRTEM result and the lamellar crystal lattice distance in Figure S5. It is well known that micropores and mesopores play a critical role in electrochemical processes, due to their capability of facilitating mass diffusion/transport (guest ion/molecule transport, and electrolyte penetration) and ensuring a high electroactive surface area [39]. Accordingly, two pore-size structures of the lamellar $K_2Co_3(P_2O_7)_2 \cdot 2H_2O$ nanocrystal whisker may affect its performance in electrochemical energy storage application in different ways.

Electrochemical properties of the as-prepared lamellar $K_2Co_3(P_2O_7)_2 \cdot 2H_2O$ nanocrystal whisker electrode in a conventional three-electrode system

The electrochemical performance of as-prepared lamellar $K_2Co_3(P_2O_7)_2 \cdot 2H_2O$ nanocrystal whisker electrode was firstly studied in a conventional three-electrode system using CV method. Figure 3a shows the CV curves of lamellar $K_2Co_3(P_2O_7)_2 \cdot 2H_2O$ nanocrystal whisker electrodes (mass loading of ~ 5 mg) in 3.0 M KOH electrolyte at different scan rates of 5–100 mV s^{-1} . As shown in Figure 3a, the shapes suggest a pseudocapacitive nature, and the Faradaic pseudocapacitive property of the lamellar $K_2Co_3(P_2O_7)_2 \cdot 2H_2O$ nanocrystal whisker may be a result from the redox reaction of Co(II) to Co(III) on the surface.

Chronopotentiometry (CP) curves of as-prepared lamellar $K_2Co_3(P_2O_7)_2 \cdot 2H_2O$ nanocrystal whisker electrode were further studied in a conventional three-electrode system at different current densities (Figure 3b). The lamellar $K_2Co_3(P_2O_7)_2 \cdot 2H_2O$ nanocrystal whisker electrode shows the symmetrical characteristics of the charging/discharging curves, which indicates its excellent electrochemical capability and the reversible redox process. The specific capacitances calculated by the discharge curves of Figure 3b are shown in Figure 3c. Based on these results, the lamellar $K_2Co_3(P_2O_7)_2 \cdot 2H_2O$ nanocrystal whisker electrode had a large specific capacitance of 1100 mF cm^{-2} at the current density of 1.0 mA cm^{-2} , and 831 mF cm^{-2} even at 5.0 mA cm^{-2} showing its potential for high power applications.

The cycling performances of the lamellar $K_2Co_3(P_2O_7)_2 \cdot 2H_2O$ nanocrystal whisker electrode at different current densities (1.0, 1.5, 2.0, 3.0 and 5.0 mA cm^{-2}) are shown in Figure 3d. It is seen that the capacity changed from 1100 mF cm^{-2} to 810 mF cm^{-2} as the current density increased from 1.0 mA cm^{-2} to 5.0 mA cm^{-2} . What is more, the cycle remained stable at each current

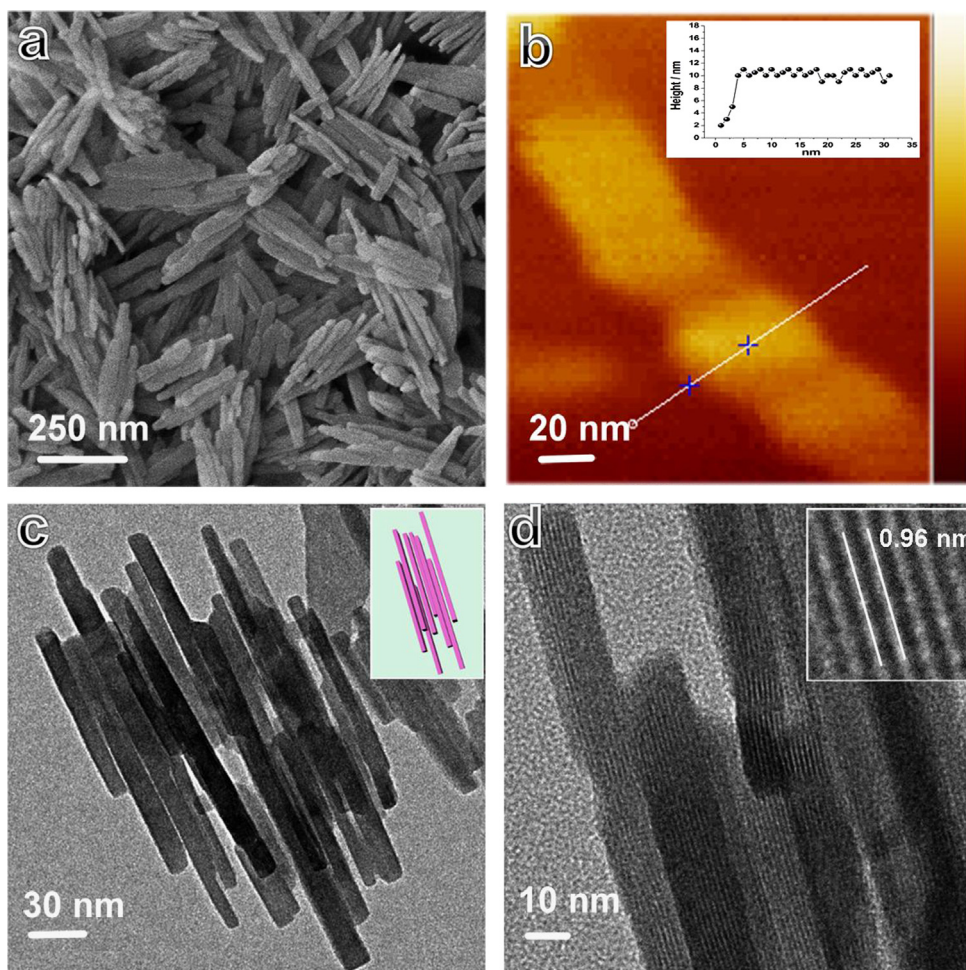


Figure 2 (a) SEM image of as-prepared samples, (b) AFM image, (c) TEM image, and the model image of overlapping $K_2Co_3(P_2O_7)_2 \cdot 2H_2O$ nanocrystal whiskers (Inset), and (d) HRTEM image, and the large magnification image (Inset).

density, further confirming the good rate stability of the electrode materials.

High electrical conductivity is crucial for supercapacitor electrode materials. To identify the exact electrical conductivity of the lamellar $K_2Co_3(P_2O_7)_2 \cdot 2H_2O$ nanocrystalline whisker electrode, we measured the electrochemical impedance spectra (EIS) spectrum of the lamellar $K_2Co_3(P_2O_7)_2 \cdot 2H_2O$ nanocrystal whisker electrode at room temperature in the frequency range of $0.01\text{-}10^5$ Hz under open-circuit conditions, as shown in [Figure S7](#). We propose an equivalent circuit to fit the impedance curve in the inset of [Figure S7](#), which is used to simulate the circuit employed in a working supercapacitor. The EIS spectrum can be fitted by a bulk solution resistance R_s , a charge-transfer R_{ct} and a pseudocapacitive element C_p from the existing redox process, and the double-layer capacitance (CPE). What is more, the charge-transfer resistance R_{ct} of the lamellar $K_2Co_3(P_2O_7)_2 \cdot 2H_2O$ nanocrystalline whisker electrode calculated by ZSimpWin software was as low as 8.9Ω which clearly demonstrates the reduced charge-transfer resistance of as-prepared the lamellar $K_2Co_3(P_2O_7)_2 \cdot 2H_2O$ nanocrystalline whisker, an effect possibly due to the novel surface-interface, which may decrease the electrode polarization and increase its electrochemical active sites.

The galvanostatic charge-discharge curves and specific capacitances of the as-prepared graphene nanosheets are shown in

[Figure S8](#). The specific capacitance of as-prepared graphene nanosheets is 250 mF cm^{-2} at 1.0 mA cm^{-2} . So the mass ratio between the positive and negative electrode in the device is set to 1:4.5.

Electrochemical properties of the as-prepared flexible solid-state asymmetric supercapacitor

The flexible solid-state asymmetric micro-supercapacitor (denoted by micro-device) was then fabricated *via* an inkjet printing method, and the structure scheme of device is illustrated in [Figure 4a](#). Silver ink was printed on the PET substrate for active materials (Lamellar $K_2Co_3(P_2O_7)_2 \cdot 2H_2O$ nanocrystalline whisker, and Graphene nanosheets). In [Figure S9](#), we provide SEM images of the cross-section of the electrodes to understand the structure of the as-prepared flexible electrodes with different view directions. It is seen that the thickness of the as-prepared lamellar $K_2Co_3(P_2O_7)_2 \cdot 2H_2O$ nanocrystal whisker electrode is about 230 nm, while the thickness of the layer of as-prepared graphene nanosheet electrode is about 1200 nm. The gap between the layer of active materials and the PET substrate is caused by the strong X ray electron beam from the SEM machine. Gel electrolyte (KOH/PVA) was spread on the active

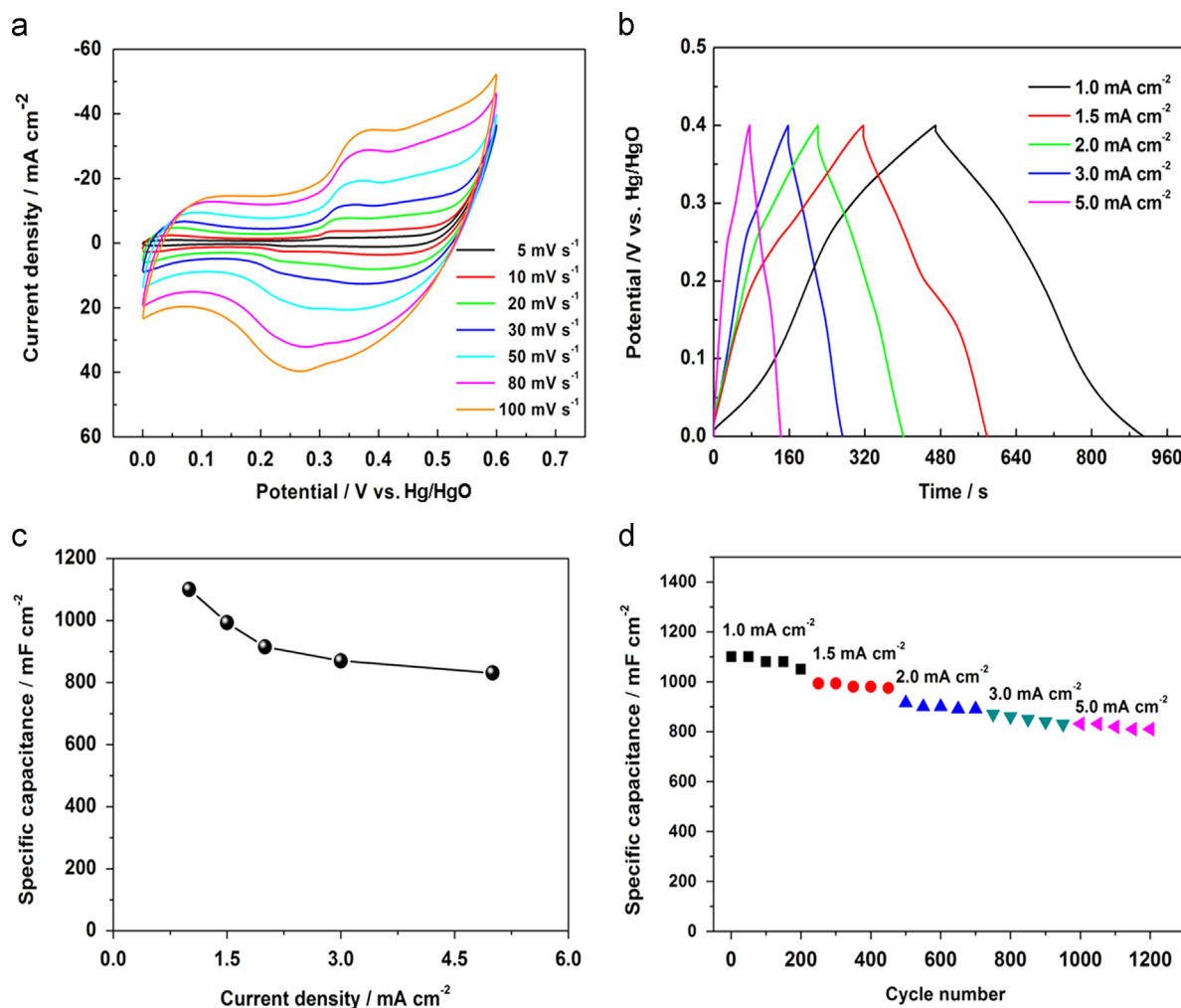


Figure 3 In a conventional three-electrode system: (a) CV experiments within a 0.0–0.60 V range at a scan rate 5–100 $mV\ s^{-1}$ were performed on the lamellar $K_2Co_3(P_2O_7)_2 \cdot 2H_2O$ nanocrystal whisker electrodes in 3.0 M KOH electrolytes at room temperature, (b) the galvanostatic charge-discharge curves of lamellar $K_2Co_3(P_2O_7)_2 \cdot 2H_2O$ nanocrystal whisker electrodes during current densities were 1.0–5.0 $mA\ cm^{-2}$, (c) specific capacitances of $K_2Co_3(P_2O_7)_2 \cdot 2H_2O$ nanocrystal whisker electrodes derived from the discharging curves at the current density of 1.0–5.0 $mA\ cm^{-2}$, and (d) charge/discharge cycling test at different current densities from 1.0 to 5.0 $mA\ cm^{-2}$.

materials manually and was covered by another PET in order to prevent the loss of water in the gel electrolyte. Figure 4b shows CV curves of the micro-device with different cell voltages varying from 0.0–0.50 V to 0.0–1.07 V. The presence of the weak redox peaks (when the operating potential is 0.50 V in the region between 0.0 and 0.50 V) indicates that the pseudocapacitive properties of the cell originate from the positive electrode (the lamellar $K_2Co_3(P_2O_7)_2 \cdot 2H_2O$ nanocrystal whisker). When increasing the operating potential to 1.07 V, we can find the largest surrounding area from the corresponding CV curve which means this is the potential at which most Faradaic reactions occurred. Moreover, the charge-discharge curves of the micro-device at a current density of 60 $mA\ cm^{-3}$ held nearly symmetric at an operating potential of $-1.07\ V$ (Figure 4c). It means the micro-device exhibits ideal capacitive characteristics with a rapid I-U response due to a small equivalent series resistance [40]. Figure 4d shows a variety of the specific capacitances of the micro-device calculated based on the discharge curves of Figure 4c. The specific capacitance increased from 0.67 to 5.31 $F\ cm^{-3}$ as the operating potential

increased from 0.5 to 1.07 V. According to the equation $E = CU^2/2$, the amount of the stored energy and delivered power of the micro-device (the potential window is 0.0–1.07 V) can increase by at least 36-fold compared with those with the potential window of 0–0.50 V. As a result of the increased Faradaic reactions and the large voltage window, considerably improved energy density and powder density can be obtained.

CV curves of the flexible micro-device (5–100 $mV\ s^{-1}$) were also measured as shown in Figure 5a (the potential window is 0.0–1.07 V). The micro-device displayed a quasi-rectangular CV geometry with fewer obvious redox peaks, indicating a combination of both pseudocapacitive and EDLC properties at all scan rates. Interestingly, the shape of the CV curve can still be well maintained even at the scan rate of 100 $mV\ s^{-1}$, which indicates a good rate capability of the micro-device.

Galvanostatic charge-discharge curves of the micro-device at different current densities are shown in Figure 5b. The specific capacitance reached 6.0 $F\ cm^{-3}$ at a current density of 10 $mA\ cm^{-3}$, and other specific capacitances were also plotted in Figure 5c. The micro-device exhibited good rate capability

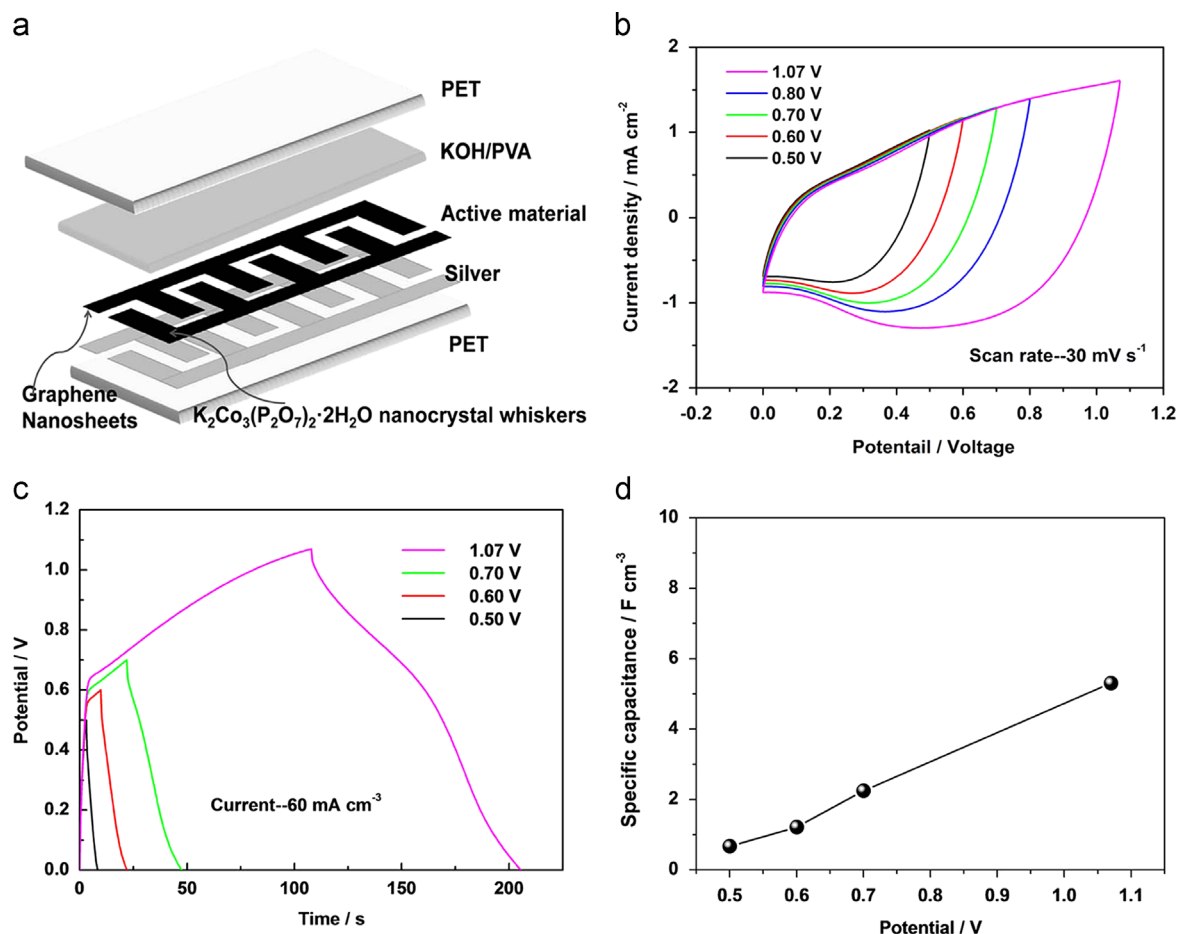


Figure 4 (a) Schematic view of the printed flexible micro-device, (b) CV curves, (c) galvanostatic charge-discharge curves, and (d) specific capacitances of the micro-device with the increase of the potential window.

(68.1% retention at 100 mA cm^{-3}). The energy and power densities of the micro-device measured at different scan rates are shown in Figure 5d. With an operating potential of 1.07 V , a maximum volumetric energy density of $0.96 \text{ mW h cm}^{-3}$ was achieved. Additionally, the maximum power density of the micro-device was 54.5 mW cm^{-3} at 100 mA cm^{-3} . These values of the as-assembled micro-device are comparable to those of other reported devices as shown in Figure S10 [41-52]. The maximum energy density of our micro-device is larger than most devices in Figure S10, but is smaller than PANI// $\text{WO}_x\text{@MoO}_x$ ($1.91 \text{ mW h cm}^{-3}$) [46] and $\text{Ni}(\text{OH})_2\text{//FDU15}$ ($2.16 \text{ mW h cm}^{-3}$) [49]. Additionally, the maximum power density of the micro-device is much higher than that of the recently reported devices: NiO//C [41], ZnO@MnO_2 [45] and $\text{ZnO@MnO}_2\text{//Graphene}$ [47], but lower than that of other devices in Figure S10. The results above confirm that the lamellar $\text{K}_2\text{Co}_3(\text{P}_2\text{O}_7)_2 \cdot 2\text{H}_2\text{O}$ nanocrystalline whisker is very promising as a high energy-density anode material for all-solid-state asymmetric micro-supercapacitors. The improved performance can be attributed to the effect of high ion permeability of the layered crystal structure, the abundant ion and electron pathways.

Figure 5e shows the cycling performance of the flexible micro-device at different current densities ($10, 16, 60, 80,$ and 100 mA cm^{-3}). When the current density changed from 10 mA cm^{-3} to 100 mA cm^{-3} , the specific capacitance changed from 6.0 F cm^{-3} to 3.9 F cm^{-3} . Interestingly, the stable cycling

performance of the micro-device was also maintained at each current density, which further confirmed its good rate stability. 5000 charge-discharge cycling tests were carried out to examine the long-term cycle ability of the micro-device (Figure 5f). During the cycling process at a current density of 10 mA cm^{-3} , only a small decay of the capacitance was observed. And the decay could have resulted from the consumption of the gel electrolyte due to an irreversible reaction from active materials and electrolytes [39]. After 5000 cycles, the specific capacitance of the micro-device is still approximately 94.4% of its initial capacitance (6.0 F cm^{-3}), which strongly proves the good cycling performance of the micro-device.

The device has been bended with different angles ($30^\circ, 60^\circ, 90^\circ,$ and 180° , Figure S11) and corresponding electrochemical properties have been measured, with an aim to test the flexibility of the micro-device. CV measurements were conducted at the scan rate of 30 mV s^{-1} with various bending angles (Ranging from 0° to 180°). As is shown in Figure S12a, the CV curves with different bending angles barely changed. Galvanostatic charge-discharge curves at 60 mA cm^{-3} with various bending angles are shown in Figure S12b, from which the corresponding specific capacitance ratios are found to be in the range of 134-117% (Figure S12c). By comparing the specific capacitance at the bent states ($30^\circ\text{-}180^\circ$) with the normal state (0°), we can draw the conclusion that the flexible device under bent conditions has even larger specific capacitance. This enhancement may be caused by the improved ion and

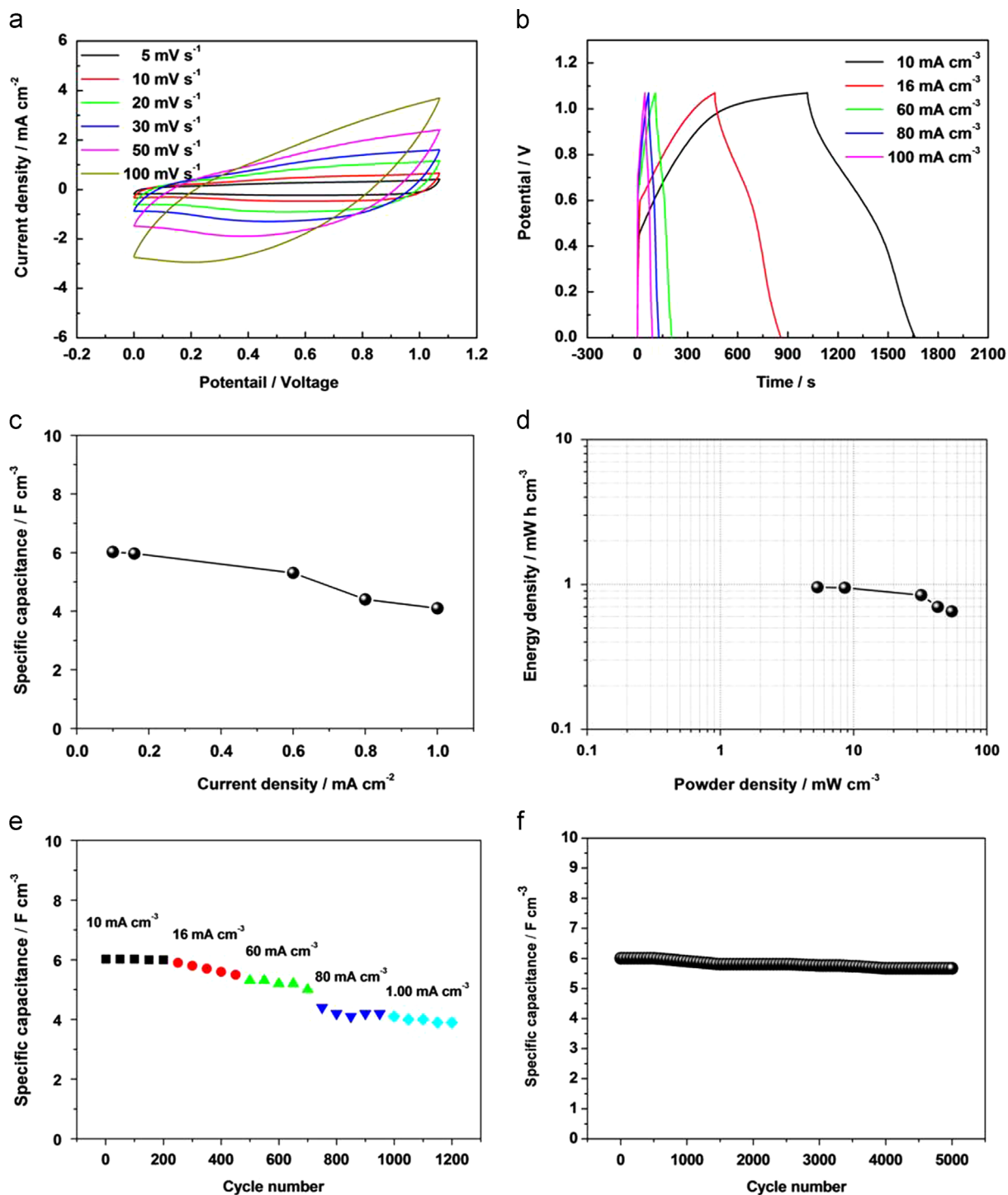


Figure 5 (a) CV curves with scan rates between 5 and 100 mV s⁻¹, (b) galvanostatic charge-discharge curves at current densities ranging from 10 to 100 mA cm⁻³ of the micro-device in the potential window of 0.0-1.07 V; (c) the specific capacitance was calculated based on the data in Figure 5b, (d) Ragone plots of the micro-device based on the full cell, (e) cycling performance of the micro-device at different current densities, and (f) cycling performance of the micro-device at 10 mA cm⁻³ for 5000 cycles.

electrolyte diffusion under bent conditions. The cycle stability under severely bent conditions is also an important parameter for flexible devices. With the curvature ranging from 0° to 180°, over 1000 cycles at the current density of 10 mA cm⁻³ were tested respectively, and the results are shown in Figure S12d, which further demonstrates the excellent mechanical stability of the micro-device [40]. Notably, after the bending and cycling

of the device, the specific capacitance was maintained and even enhanced.

Conclusions

In summary, a high-performance flexible all-solid-state asymmetric micro-supercapacitor based on lamellar K₂Co₃

$(P_2O_7)_2 \cdot 2H_2O$ nanocrystal whiskers/graphene nanosheets was fabricated using a simple inkjet printing method. The micro-device offered excellent cycling stability (retaining 94.4% of capacitance after 5000 cycles), and larger energy density (0.96mWhcm^{-3}) than most previous solid-state micro-supercapacitors. In addition, the flexible device showed excellent mechanical flexibility with a bending angle in the range of 0° - 180° . Due to the eco-friendly nature of material synthesis and simple device fabrication process, the micro-device can be integrated into many portable devices such as power-on-chip systems and roll-up display panels. Other applications are also anticipated by exploiting the advantages of flexibility and high energy density of this flexible solid-state asymmetric micro-supercapacitor endowed by both the materials and the device configuration design.

Acknowledgments

We acknowledge financial support from the National Key Basic Research Program of China (973 Program, 2014CB648300), the Program for New Century Excellent Talents in University (grant No. NCET-13-0645, and NCET-13-0872), the National Natural Science Foundation of China (21201010, 21422402, 20904024, 51173081, 61136003, 61106036, and U1304504), the Program for Innovative Research Team (in Science and Technology) in University of Henan Province (14IRTSTHN004), the Science & Technology Foundation of Henan Province (14B150001), the Natural Science Foundation of Jiangsu Province (BK20140060, BK20130037 and BM2012010), Specialized Research Fund for the Doctoral Program of Higher Education (20133223110008), the Ministry of Education of China (IRT1148), the Program for Graduate Students Research and Innovation of Jiangsu Province (CXZZ12-0454), the Priority Academic Program Development of Jiangsu Higher Education Institutions (PAPD), the Six Talent Plan (2012XCL035) Qing Lan Project of Jiangsu Province, and Synergetic Innovation Center for Organic Electronics and Information Displays.

Appendix A. Supporting information

Supplementary data associated with this article can be found in the online version at <http://dx.doi.org/10.1016/j.nanoen.2015.04.034>.

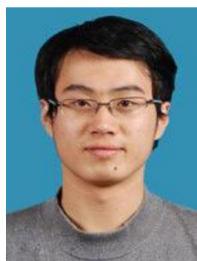
References

- [1] J. Ren, L. Li, C. Chen, X. Chen, Z. Cai, L. Qiu, Y. Wang, X. Zhu, H.S. Peng, *Adv. Mater.* 25 (2013) 1155-1159.
- [2] C.Z. Yuan, H.B. Wu, Y. Xie, X.W. (David) Lou, *Angew. Chem., Int. Ed.* 53 (2014) 1488-1504.
- [3] L. Peng, X. Peng, B. Liu, C.Z. Wu, Y. Xie, G.H. Yu, *Nano Lett.* 13 (2013) 2151-2157.
- [4] M.-R. Gao, Y.-F. Xu, J. Jiang, S.-H. Yu, *Chem. Soc. Rev.* 42 (2013) 2986-3017.
- [5] Y.G. Wang, Y.Y. Xia, *Electrochim. Acta* 51 (2006) 3223-3227.
- [6] W. Li, K. Xu, B. Li, J. Sun, F. Jiang, Z.S. Yu, R. Zou, Z.G. Chen, J.Q. Hu, *ChemElectroChem* 1 (2014) 1003-1008.
- [7] L.Q. Mai, A. Minhas-Khan, X. Tian, K.M. Hercule, Y.-L. Zhao, X. Lin, X. Xu, *Nat. Commun.* 4 (2014) 2923.
- [8] Q.F. Wang, X.F. Wang, B. Liu, G. Yu, X.J. Hou, D. Chen, G.Z. Shen, *J. Mater. Chem. A* 1 (2013) 2468-2473.
- [9] X.F. Wang, B. Liu, Q.F. Wang, W.F. Song, X.J. Hou, D. Chen, Y.B. Cheng, G.Z. Shen, *Adv. Mater.* 25 (2013) 1479-1486.
- [10] C.Z. Meng, C.H. Liu, L.Z. Chen, C.H. Hu, S.S. Fan, *Nano Lett.* 10 (2010) 4025-4031.
- [11] H.C. Gao, F. Xiao, C.B. Ching, H.W. Duan, *ACS Appl. Mater. Interfaces* 4 (2012) 7020-7026.
- [12] Z.S. Wu, Y. Sun, Y.Z. Tan, S.B. Yang, X.L. Feng, K. Mullen, *J. Am. Chem. Soc.* 134 (2012) 19532-19535.
- [13] Y.H. Xiao, A.Q. Zhang, S.J. Liu, J.H. Zhao, S.M. Fang, D.Z. Jia, F. Li, *J. Power Sources* 219 (2012) 140-146.
- [14] J. Xu, Q.F. Wang, X.W. Wang, Q.Y. Xiang, B. Liang, D. Chen, G.Z. Shen, *ACS Nano* 7 (2013) 5453-5462.
- [15] W. Chen, R.B. Rakhi, L.B. Hu, X. Xie, Y. Cui, H.N. Alshareef, *Nano Lett.* 11 (2011) 5165-5172.
- [16] P. Simon, Y. Gogotsi, *Nat. Mater.* 7 (2008) 845-854.
- [17] X. Cao, Y. Shi, W. Shi, G. Lu, X. Huang, Q. Yan, Q. Zhang, H. Zhang, *Small* 7 (2011) 3163-3168.
- [18] X. Lang, A. Hirata, T. Fujita, M. Chen, *Nat. Nanotechnol.* 6 (2011) 232-236.
- [19] A.S. Arico, P. Bruce, B. Scrosati, J.-M. Tarascon, W. van Schalkwijk, *Nat. Mater.* 4 (2005) 366-377.
- [20] L. Yang, S. Cheng, Y. Ding, X.B. Zhu, Z.L. Wang, M.L. Liu, *Nano Lett.* 12 (2012) 321-325.
- [21] L.L. Zhang, X. Zhao, M.D. Stoller, Y.W. Zhu, H.X. Ji, S. Murali, Y.P. Wu, S. Perales, B. Clevenger, R.S. Ruoff, *Nano Lett.* 12 (2012) 1806-1812.
- [22] Y.F. Xu, M.G. Schwab, A.J. Strudwick, I. Hennig, X.L. Feng, Z.S. Wu, K. Müllen, *Adv. Energy Mater.* 3 (2013) 1035-1040.
- [23] X.B. Ji, P.M. Hallam, S.M. Houssein, R. Kadara, L. Lang, C.E. Banks, *RSC Adv.* 2 (2012) 1508-1515.
- [24] Y.F. Xu, I. Hennig, D. Freyberg, A.J. Strudwick, M.G. Schwab, T. Weitz, K.C.-P. Cha, *J. Power Sources* 248 (2014) 483-488.
- [25] P. Chen, H. Chen, J. Qiu, C.W. Zhou, *Nano Res.* 3 (2010) 594-603.
- [26] A. Chiolerio, S. Bocchini, S. Porro, *Adv. Funct. Mater.* 24 (2014) 3375-3383.
- [27] C. Chen, W. Chen, J. Lu, D. Chu, Z. Huo, Q. Peng, Y.D. Li, *Angew. Chem., Int. Ed.* 48 (2009) 4816-4819.
- [28] C. Morgovan, E. Marian, A. Iovi, I. Bratu, G. Borodi, *Rev. Chim.* 60 (2009) 1282.
- [29] I.S. Cho, D.W. Kim, S. Lee, C.H. Kwak, S.T. Bae, J.H. Noh, S.H. Yoon, H.S. Jung, D.W. Kim, K.S. Hong, *Adv. Funct. Mater.* 18 (2008) 2154.
- [30] D.Q. Liu, X. Wang, X.B. Wang, W. Tian, J.W. Liu, C.Y. Zhi, D.Y. He, Y. Bando, D. Golberg, *J. Mater. Chem. A* 1 (2013) 1952.
- [31] H. Pang, Z. Yan, W. Wang, J. Chen, J.S. Zhang, H.H. Zheng, *Nanoscale* 4 (2012) 5946-5953.
- [32] H. Pang, Y.Y. Liu, J. Li, Y.H. Ma, G.C. Li, Y.N. Ai, J. Chen, J.S. Zhang, H.H. Zheng, *Nanoscale* 5 (2013) 503-507.
- [33] H. Pang, Z. Yan, Y. Ma, G. Li, J. Chen, J. Zhang, W. Du, S.J. Li, *J. Solid State Electrochem.* 17 (2013) 1383-1391.
- [34] H. Wen, M.H. Cao, G.B. Sun, W.G. Xu, D. Wang, X.Q. Zhang, C.W. Hu, *J. Phys. Chem. C* 112 (2008) 15948-15955.
- [35] Y. Zhang, C. Zhao, X. Dai, H. Lin, B. Cui, J.B. Li, *J. Power Sources* 243 (2013) 908-912.
- [36] L.R. Hou, L. Lian, D.K. Li, J.D. Lin, G. Pang, L.H. Zhang, X.G. Zhang, Q. Zhang, C.Z. Yuan, *RSC Adv.* 3 (2013) 21558-21562.
- [37] S.M. Wang, H. Pang, S.S. Zhao, W.F. Shao, N. Zhang, J. Zhang, J. Chen, S.J. Li, *RSC Adv.* 4 (2014) 340-347.
- [38] H. Pang, S. Wang, W. Shao, S. Zhao, B. Yan, X. Li, S. Li, J. Chen, W. Du, *Nanoscale* 5 (2013) 5752-5757.
- [39] D. Wang, W. Ni, H. Pang, Q. Lu, Z. Huang, J. Zhao, *Electrochim. Acta* 55 (2010) 6830-6835.

- [40] L.-F. Chen, Z.-H. Huang, H.-W. Liang, Q.-F. Guan, S.-H. Yu, *Adv. Mater.* 25 (2013) 4746-4752.
- [41] L.N. Gao, X.F. Wang, Z. Xie, W.F. Song, L.J. Wang, X. Wu, F.Y. Qu, D. Chen, G.Z. Shen, *J. Mater. Chem. A* 1 (2013) 7168-7173.
- [42] M.F. El-Kady, V. Strong, S. Dubin, R.B. Kaner, *Science* 335 (2012) 1326.
- [43] X.H. Lu, G.M. Wang, T. Zhai, M.H. Yu, S.L. Xie, Y.C. Ling, C.L. Liang, Y.X. Tong, Y. Li, *Nano Lett.* 12 (2012) 5376.
- [44] X.H. Lu, M. Yu, T. Zhai, G. Wang, S. Xie, T. Liu, C. Liang, Y. Tong, Y. Li, *Nano Lett.* 13 (2013) 2628.
- [45] P. Yang, X. Xiao, Y. Li, Y. Ding, P. Qiang, X. Tan, W. Mai, Z. Lin, W. Wu, T. Li, H. Jin, P. Liu, J. Zhou, C.P. Wong, Z.L. Wang, *ACS Nano* 7 (2013) 2617.
- [46] X. Xiao, X. Peng, H. Jin, T. Li, C. Zhang, B. Gao, B. Hu, K. Huo, J. Zhou, *Adv. Mater.* 25 (2013) 5091.
- [47] W. Zilong, Z. Zhu, J. Qiu, S. Yang, *J. Mater. Chem. C* 2 (2014) 1331.
- [48] X.H. Lu, Y.X. Zeng, M.H. Yu, T. Zhai, C.L. Liang, S.L. Xie, M.-S. Balogun, Y.X. Tong, *Adv. Mater.* 26 (2014) 3148-3155.
- [49] X.L. Dong, Z.Y. Guo, Y.F. Song, M.Y. Hou, J.Q. Wang, Y.G. Wang, Y.Y. Xia, *Adv. Funct. Mater.* 24 (2014) 3405-3412.
- [50] X.F. Wang, B. Liu, R. Liu, Q.F. Wang, X.J. Hou, D. Chen, R.M. Wang, G.Z. Shen, *Angew. Chem. Int. Ed.* 53 (2014) 1849-1853.
- [51] X.H. Lu, M.H. Yu, G.M. Wang, T. Zhai, S.L. Xie, Y.C. Ling, Y.X. Tong, Yat Li, *Adv. Mater.* 25 (2013) 267-272.
- [52] Z.B. Lei, J.T. Zhang, X.S. Zhao, *J. Mater. Chem.* 22 (2012) 153.



Huan Pang received his Ph. D. degree from Nanjing University in 2011. He then founded his research group in Anyang Normal University where he was appointed as a distinguished professor in 2013. Now, he also joined Yangzhou University as a distinguished professor. His research interests include the development of inorganic semiconductor nanostructures and their applications in flexible electronics and printable electronics.



Yi-Zhou Zhang received his B.S.c from Department of Chemistry and Chemical Engineering of Nanjing University in 2010, after which he has been studying as a PhD candidate under Professor Wei Huang's and Professor Wen-Yong Lai's supervision. His current research focuses on flexible and stretchable energy storage devices with the special focus on supercapacitors. He is also interested in using inkjet printing as a fabrication tool for electronics.



Wen-Yong Lai is a professor at Nanjing University of Posts and Telecommunications. He received his Ph.D from Fudan University in 2007. He then joined the Key Laboratory for Organic Electronics & Information Displays and Institute of Advanced Materials (IAM), Nanjing University of Posts & Telecommunications. His research mainly focuses on the design, synthesis, and application of organic & polymer optoelectronic materials for organic/plastic electronics. He is also interested in the exploration of novel materials and processes for printed/flexible electronics.



Zheng Hu received his BS (1985) and Ph.D. (1991) degrees in physics from Nanjing University. After two-year's postdoctoral research in Department of Chemistry, he became an associate professor in 1993, and subsequently acquired the professor position in 1999, and Cheung Kong Scholar professor in 2007. He is the owner of the highly competitive NSFC fund for outstanding young scientists of China (2005). As a guest scientist, he visited Research Center of Karlsruhe (Germany), University of Cambridge (UK), and MIT (USA) for two years. Hu is engaged in the research field of physical chemistry and materials chemistry addressing the growth mechanism, materials design and energy applications of a range of nano-/mesostructured materials, especially the carbon-based materials and group III nitrides.



Wei Huang received his PhD degree from Peking University in 1992. In 1993, he began his postdoctoral research in the National University of Singapore (NUS) and then taught at the Department of Chemical Engineering, NUS. In 2001, he was appointed as Chair Professor with Fudan University, where he founded and chaired the Institute of Advanced Materials (IAM). In 2006, he was appointed as Deputy President of the Nanjing University of Posts and Telecommunications. 2012, he assumed his duty as the President of the Nanjing Tech University (NanjingTech). He was elected as Academician of the Chinese Academy of Sciences in 2011. His research interests include organic/plastic/flexible (opto)electronics, nanomaterials, nanotechnology, etc.